Journal of Statistical Physics, Vol. 68, Nos. 1/2, 1992

The Semiclassical Limit of a Quantum Fermi Accelerator

G. Chu[1] **and Jorge V. José**[1]

Received December 3, 1991; final March 9, 1992

A classical Fermi accelerator model (FAM) is known to show chaotic behavior. The FAM is defined by a free particle bouncing elastically from two rigid walls, one fixed and the other oscillating periodically in time. The central aim of this paper is to connect the quantum and the classical solutions to the FAM in the semiclassical limit. This goal is accomplished using a finite inverted parametric oscillator (FIPO), confined to a box with *fixed walls*, as an alternative representation of the FAM. In the FIPO representation, an explicit correspondence between classical and quantum limits is accomplished using a Husimi representation of the quasienergy eigenfunctions.

KEY WORDS: Fermi accelerator model; Liouville transform; chaos; quantum time-periodic Hamiltonian; semiclassical limit; Floquet operator; quasienergy spectrum; Husimi distribution; scars;

1. INTRODUCTION

An important question of contemporary interest is to find out the *quantum manifestations of classical chaos* (QMCC). A significant amount of work has been directed at finding answers to this question and a general framework is emerging where aspects of the QMCC are becoming established. Analyses of the statistical properties of the energy level separations of time-independent Hamiltonians have led to explicit differences between those with an integrable and those with a nonintegrable classical counterpart (e.g., ref. 1). The framework in which these classifications have been made is provided by the phenomenological Gaussian ensembles of *random matrix theory* (RMT), introduced by Wigner and Dyson to account for the physics of complex nuclei[2] (See ref. 3 for a recent review). When the Hamiltonians are time-periodic, the quasienergy spectra have been found

[1] Department of Physics, Northeastern University, Boston, Massachusetts 02115.

0022-4715/92/0700-0153$06.50/0

to follow the circular ensembles of RMT.[4,5] In many of these studies, though not all,[6,7] a direct and explicit connection between the classical and quantum solutions has not been provided. It is, however, quite important to be able to "see" how the quantum solutions merge to the classical ones in the semiclassical limit.

It has become the norm in the field of QMCC to study specific quantum mechanical models known to be chaotic in the classical limit. One such model is the Fermi accelerator model (FAM), which has been extensively studied classically[8] and to some extent quantum mechanically.[4,9] This model was introduced by Fermi to explain the origin of the high-energy cosmic rays bombarding the earth.[10] The FAM was one of the first models to study chaotic behavior in a classical two-degrees-of-freedom system. The quantum study of the model has revealed novel features of the fluctuations in the quasienergy spectrum. The nearest neighbor quasienergy statistics interpolate between Poisson and Wigner-type distributions as $\hbar$ goes from large to small.[4,9] A direct connection between the classical and quantum solutions, although it was attempted in ref. 9, has not been presented. Achieving this connection is the central point of this paper. One of the main problems in connecting the quantum with the classical problem in phase space is to have an appropriate representation of both treatments in terms of bona fide canonically conjugate variables. We are able to carry out this connection by using an alternative representation of the FAM in terms of a finite inverted parametric oscillator model (FIPO). In the FIPO representation we are then able to connect the classical and the quantum solutions. We present several examples of specific classical periodic orbits with their quantum counterparts.

This paper is organized as follows: first we present the transformation maps of the FAM to the FIPO both in the classical and quantum cases. We consider the specific wall oscillation rule used in refs. 4 and 9 to obtain explicit solutions to the FAM problem. For this oscillation law an almost complete quantum mechanical integration of the FAM is possible. In the FIPO representation one gets a model with two δ-kicked inverted oscillators. A direct comparison between the classical and quantum approaches can then be carried out, for it is found that the kicks occur at integer or half-integer periods of the oscillating wall. By contrast, in the classical study of the FAM the maps obtained relate particle collisions with the moving wall that do not necessarily occur at the period of the oscillating wall. This is an important difference, since the quantum analysis is done using the quantum Floquet operator, which is defined at the wall period. In Section 3 we present an analytic analysis of a set of particular periodic orbits in the classical limit. The quantum problem is formulated in Section 4, and in Section 5 the bulk of our numerical solutions is presented.

It is in Section 5 where we make the connection between the selected set of classical orbits and quantum quasienergy eigenfunctions, including scarred periodic orbits. We conclude in Section 6 with a brief recap of the main results of the paper and a discussion of some open problems left for the future.

2. CANONICAL TRANSFORMATION

The Fermi accelerator model (FAM) is defined by the Hamiltonian

$$H_{\mathrm{FAM}} = \frac{1}{2} m \left(\frac{dy(\tau)}{d\tau} \right)^2; \qquad 0 \leqslant y(\tau) \leqslant l_0 S(\tau) \tag{1}$$

with l_0 the minimum box size and $S(\tau)$ a periodic function of time τ, i.e., $S(\tau + \tau_0) = S(\tau)$. Previously, the study of the model in the classical limit used as dynamical variables the normalized velocity of the particle v_n and the position of the wall before the nth collision ϕ_n. The resulting two-dimensional area-preserving map, $(v_{n+1}, \phi_{n+1}) = T(v_n, \phi_n)$, for specific $S(\tau)$ laws, was then studied using standard dynamical system theory.[8] Periodic and chaotic solutions were found whenever $S(\tau)$ is such that the moving wall does not move with constant velocity, since otherwise the solutions are nonchaotic. The problem of connecting these classical solutions to their quantum counterparts is that the particle can have many collisions with the moving wall before it hits the fixed wall again. By contrast, in the quantum problem, as will be discussed later, the solutions are obtained by calculating the time evolution operator at a period of the oscillating wall. One could try and solve the equation of motion resulting from Eq. (1) for $y(\tau)$ at a period. Instead, we choose to change the representation of the problem to one where we can achieve the goal of expressing the classical solutions at a period with classical and quantum maps that are clearly connected to each other.

The transformation is carried out by using the well-known Liouville transformation[11]

$$\begin{aligned} t &= \int_0^\tau \frac{d\tau'}{S^2(\tau')} \\ x &= \frac{y}{S(\tau)} \end{aligned} \tag{2}$$

This is a nonlinear transformation in time and a rescale transformation in space. Substituting this transformation in Eq. (1), after using the chain rule, we get the finite parametric oscillator equation of motion

$$\frac{d^2}{dt^2} x(t) + \omega^2(t)\, x(t) = 0; \qquad 0 \leqslant x(t) \leqslant l_0 \tag{3}$$

with angular frequency

$$\omega^2(t) = \frac{d}{dt}\left(\frac{1}{\theta(t)}\frac{d\theta(t)}{dt}\right) - \left(\frac{1}{\theta(t)}\frac{d\theta(t)}{dt}\right)^2 \tag{4}$$

To avoid confusion, we are calling $S(t) = S(t(\tau)) = \theta(t)$ hereafter. Note that $\omega^2(t + T_0) = \omega^2(t)$, where T_0 is defined by

$$T_0 = \int_0^{\tau_0} \frac{d\tau}{S^2(\tau)}$$

As will be seen later, for the specific form of $S(\tau)$ in which we are interested, one gets a finite *inverted* parametric oscillator (FIPO), and for this reson we will refer to this representation as the FIPO model.

By carrying out this transformation, the time-dependent boundary condition present in the FAM has been replaced by a fixed wall boundary condition problem. Of course, since the FAM is not integrable, the FIPO is also not integrable. In fact, we can see that if the FIPO were defined in an infinite box, one could use standard classical Floquet theory to perturbatively obtain its solutions. Nevertheless, as we shall see later, it is in the FIPO representation that we are able to connect its classical to its quantum solutions.

The Hamiltonian defining the FIPO is given by

$$H_{\text{FIPO}} = \frac{p^2}{2m} + \frac{1}{2} m\omega^2(t)\, x^2; \qquad 0 \leqslant x(t) \leqslant l_0 \tag{5}$$

with momentum $p = m\dot{x}$. Note that in this representation p and x are bona fide canonically conjugate variables and thus we can use standard canonical quantization rules to write down the quantum FIPO Schrödinger equation problem as

$$\begin{aligned} i\hbar \frac{\partial}{\partial t}\Psi(x, t) &= -\frac{\hbar^2}{2m}\frac{\partial^2}{\partial x^2}\Psi(x, t) + \frac{1}{2} m\omega^2(t)\, x^2 \Psi(x, t) \\ \Psi(x = 0, t) &= \Psi(x = l_0, t) = 0 \\ \int_0^{l_0} |\Psi(x, t)|^2\, dx &= 1 \end{aligned} \tag{6}$$

To check that everything works out as it should, we go now from the quantum FIPO to the quantum FAM. In so doing we use the unitary transformation that preserves the wave function normalization condition,

$$\Phi(y, \tau) = \frac{1}{[\theta(t)]^{1/2}} \exp\left(i \frac{m}{2\hbar\theta(t)} \frac{d\theta(t)}{dt} x^2\right) \Psi(x, t) \tag{7}$$

With this unitary transformation for the wave function, together with the inverse transformation of (2), and using again the chain rule,

$$\begin{aligned} \tau &= \int_0^t \theta^2(t')\, dt' \\ y &= \theta(t)\, x \end{aligned} \tag{8}$$

we arrive at the Schrödinger equation for $\Phi(y, \tau)$, together with its boundary and normalization conditions,

$$\begin{aligned} i\hbar \frac{\partial}{\partial \tau} \Phi(y, \tau) &= -\frac{\hbar^2}{2m} \frac{\partial^2}{\partial y^2} \Phi(y, \tau) \\ \Phi(y = 0, \tau) &= \Phi(y = l_0 S(\tau), \tau) = 0 \\ \int_0^{l_0 S(\tau)} |\Phi(y, \tau)|^2\, dy &= 1 \end{aligned} \tag{9}$$

This equation is defined in the frame of reference of the original time τ and coordinate y.[4] These are the equations that define the quantum mechanical FAM.

It is clear that the frequency law $\omega^2(t)$ given in Eq. (4) is the same in both the classical and quantum mechanical representations. This is a special case, though, since in the quantum mechanical study of the FIPO the path integral representation of its Green function involves an action that consists of only linear and quadratic terms. This is one of the few cases where the Green function can be expressed exactly in term of its classical action.[12] Note that the fixed wall boundary conditions presented here merely modify the calculation of the Green function to include a summation of an infinite number of images.

The Liouville transformation mentioned above has been used extensively.[13–16] In the quantum case and applied to a FAM the second transformations (7) and (8) were used recently by Seba[17] for the specific case of the periodic $\omega^2(t)$ having at least five continuous derivatives, which unfortunately is not the case of interest here. In order to have chaotic solutions, the $\omega^2(t)$ of interest in this paper has discontinuities already in its first derivative.

As mentioned above, both the classical and quantum mechanically transformed FIPO are no easier to solve than the original FAM. The important advantage of the FIPO is that it will allow us to make explicit connections between the classical and quantum problems in the semiclassical limit. To accomplish this task, however, we need to choose the

function $S(\tau)$ appropriately. It was found that in the quantum study of the FAM the problem can be solved to a significant extent by choosing[4]

$$S(\tau)=\left(1+2\omega_0\left|\mathrm{mod}[\tau,\tau_0]-\frac{\tau_0}{2}\right|\right)^{1/2} \tag{10}$$

(note that ω_0 is the parameter δ in ref. 4), shown in Fig. 1. The function $S(\tau)$ is a periodic function of τ with period τ_0, and the overall displacement of the wall is $A=[1+\omega_0\tau_0)^{1/2}-1]\,l_0$. Using Eqs. (2) and (4), the angular frequency of the corresponding FIPO is

$$\omega^2(t)=-\omega_0^2+2\omega_0\sum_{n=-\infty}^{\infty}\left\{\delta\left(t-\left(n+\frac{1}{2}\right)T_0\right)-\delta(t-nT_0)\right\} \tag{11}$$

with $T_0=\ln(1+\omega_0\tau_0)/\omega_0$. It is seen in Eq. (11) that $\omega^2(t)$ consists of a constant inverted harmonic oscillator part and two sets of periodic Dirac-δ functions, one at integer, and the other at half-integer periods.

In the remaining parts of this paper we shall discuss our results for the classical and quantum mechanical studies of the FIPO with the angular frequency given by Eq. (11).

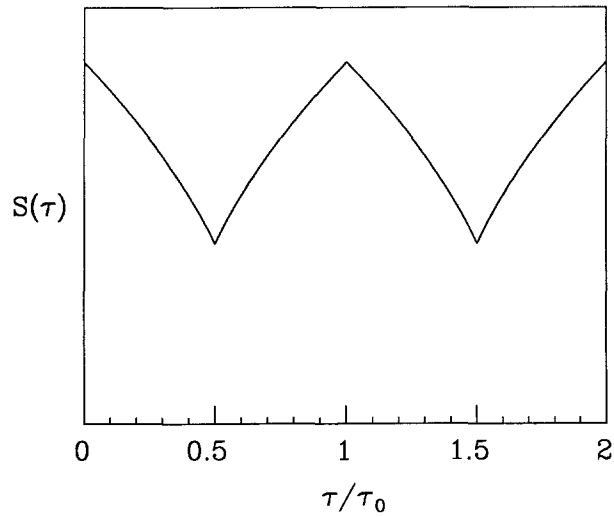

Fig. 1. Time dependence of the wall oscillation given by Eq. (10). Here $\omega_0=1$.

3. CLASSICAL STUDY

For the specific form of $\omega^2(t)$ given in Eq. (11), the Hamiltonian given in Eq. (5) reads

$$H=\frac{p^2}{2}-\frac{1}{2}\omega_0^2x^2+2\omega_0x^2\sum_{n=-\infty}^{\infty}\left\{\delta\left(t-\left(n+\frac{1}{2}\right)\right)-\delta(t-n)\right\};$$
$$0\leqslant x\leqslant 1 \tag{12}$$

Here we set $m=1$, and lengths and times are normalized by l_0 and T_0, respectively. In these units the only free parameter in the problem is ω_0, which is related to the wall oscillation amplitude of the FAM. This Hamiltonian describes the motion of a particle in the presence of an inverted harmonic oscillator potential and δ-kicked every half period. The kicks have opposite signs every half period.

When the particle does not hit the walls nor the δ-potentials, the solutions to the corresponding equations of motion can be written in the matrix form

$$\begin{pmatrix}x(t)\\p(t)\end{pmatrix}=\begin{pmatrix}\cosh(\omega_0t') & (1/\omega_0)\sinh(\omega_0t')\\ \omega_0\sinh(\omega_0t') & \cosh(\omega_0t')\end{pmatrix}\begin{pmatrix}x(t_0)\\p(t_0)\end{pmatrix}$$
$$=M_0(t-t_0)\begin{pmatrix}x(t_0)\\p(t_0)\end{pmatrix} \tag{13}$$

with $t'=t-t_0$. The time interval from t_0 to t is between full and half periods, so that the restriction $t'<1/2$ applies. The motion of the particle during this time interval is described by the Hamiltonian $H_0=p^2/2-\omega_0^2x^2/2$, with the conserved energy $E=H_0$. From the set of coupled equations given in (13) one obtains the condition

$$x(t)\,p(t_0)-x(t_0)\,p(t)=\frac{2}{\omega_0}E\sinh(\omega_0t') \tag{14}$$

for E not equal to zero. For $E=0$, $p(t_0)=\pm\omega_0x(t_0)$, so that Eq. (13) yields

$$x(t)=x(t_0)\,e^{\pm\omega_0t'} \tag{15}$$

The two equations (14) and (15) will be used later to do the analytical calculations of periodic orbits in phase space.

The collisions of the particle with the walls reverse its momentum direction at the time of collision. The effect of the collisions with the walls is given by the equation

$$\begin{pmatrix}x(t_*^+)\\p(t_*^+)\end{pmatrix}=\begin{pmatrix}1 & 0\\0 & -1\end{pmatrix}\begin{pmatrix}x(t_*^-)\\p(t_*^-)\end{pmatrix}=M_{\text{wall}}(t_*)\begin{pmatrix}x(t_*^-)\\p(t_*^-)\end{pmatrix} \tag{16}$$

where t_* is the time at which the particle hits a wall. We follow the usual convention of plus sign right after and minus sign right before a collision.

The particle is kicked by the Dirac-δ potential every full and half period. Integrating Hamilton's equations of motion for an infinitesimally small time interval before and after the full and the half periods, one gets the equations that describe how the particle gets kicked,

$$\begin{aligned}\begin{pmatrix} x(t^+) \\ p(t^+) \end{pmatrix} &= \begin{pmatrix} 1 & 0 \\ -2\omega_0 & 1 \end{pmatrix} \begin{pmatrix} x(t^-) \\ p(t^-) \end{pmatrix} = M_{\text{kick}} \left(\frac{1}{2}\right) \begin{pmatrix} x(t^-) \\ p(t^-) \end{pmatrix} \\ \begin{pmatrix} x(t^+) \\ p(t^+) \end{pmatrix} &= \begin{pmatrix} 1 & 0 \\ +2\omega_0 & 1 \end{pmatrix} \begin{pmatrix} x(t^-) \\ p(t^-) \end{pmatrix} = M_{\text{kick}}(1) \begin{pmatrix} x(t^-) \\ p(t^-) \end{pmatrix}\end{aligned} \tag{17}$$

with the first equation at half and the second at full period. The particle would be trapped in the box with a time-independent inverted harmonic oscillator potential if it were not for the kicks described by these two equations. Without the kicks the solutions to the equations of motion would be regular and thus integrable. In the special case when $x(t^+) = x(t^-) = 0$, one obtains from Eq. (17) $p(t^+) = p(t^-)$. This means that the kicks are irrelevant at $x = 0$.

One can now construct a map in phase space with Eqs. (13), (16), and (17). The points obtained by the iteration of this map describe a trajectory in phase space of an initial point according to the equations of motion. Iterating this map for a given initial point in phase space gives the positions of the particle in phase space at an integral number of periods. This map can be formally written as

$$M(1^+ \leftarrow 0^+) = M_{\text{kick}}(1) \cdot M_{\text{f}}(1^- \leftarrow \tfrac{1}{2}^+) \cdot M_{\text{kick}}(\tfrac{1}{2}) \cdot M_{\text{f}}(\tfrac{1}{2}^- \leftarrow 0^+) \tag{18}$$

This map consists of four parts. The term $M_{\text{f}}(\frac{1}{2}^- \leftarrow 0^+)$ propagates the particle freely for the first half period, while $M_{\text{kick}}(\frac{1}{2})$ indicates the kicks of the particle at a half period. After that time the $M_{\text{f}}(1^- \leftarrow \frac{1}{2}^+)$ propagates freely the particle for the second half period, whereas $M_{\text{kick}}(1)$ indicates the kicking of the particle again at an integer period. By propagating freely we mean that the particle experiences only the time-independent inverted harmonic oscillator potential confined between the two walls.

It is important to note that both $M_{\text{f}}(\frac{1}{2}^- \leftarrow 0^+)$ and $M_{\text{f}}(1^- \leftarrow \frac{1}{2}^+)$ in Eq. (18) can be formed by a product of many of the M_0 and M_{wall} matrices defined in (13) and (16). Furthermore, a series of t_*'s may have to be determined corresponding to the particle's oscillating back and forth between the two walls. For example, if the energy E_0 is such that the time for the particle to freely complete a cycle between the two walls is much smaller than 1/2, it will then hit the walls many times before it is δ-kicked. The

opposite limit is when the round-trip period is much larger than 1/2 and the particle gets kicked many times before it hits the walls. Generally speaking the map $M(1^+ \leftarrow 0^+)$ can be very complicated and a change in initial condition may result in a significant increase or decrease in the number of matrix multiplications involved.

There are a few cases that can be studied analytically and we shall consider them next. One simple case is when the energy of the particle is so small that during one period of time the particle does not hit either wall. In this case there is no effect due to the walls and the map $M(1^+ \leftarrow 0^+)$ can be calculated by evaluating the product $M_{\text{kick}}(1) \cdot M_0(1/2) \cdot M_{\text{kick}}(1/2) \cdot M_0(1/2)$. Using Eqs. (13) and (17), we get

$$M(1^+ \leftarrow 0^+) = \begin{pmatrix} e^{-\omega_0} & (1/\omega_0)(e^{-\omega_0}-1) \\ \omega_0(1-e^{-\omega_0}) & 2-e^{-\omega_0} \end{pmatrix} \tag{19}$$

The degenerate eigenvalue of this map is 1, and its eigenvector is $(x_0, \omega_0 x_0)$. Starting from these points as initial conditions, the map (19) will bring them back to their initial phase space positions after one period. These points are then fixed points phase space, i.e., periodic orbits of period -1. Note the energy of these orbits is zero. From Eq. (15) one can see that points with $x_0 > \exp(-\omega_0/2)$ are exceptions to this rule. In the present case the momentum $p_0 = \omega_0 x_0$ is taken as positive. Then if $x(t_0) > \exp(-\omega_0/2)$, after the first half period of free propagation we will have $x(t) > 1$. This means that the particle has hit the wall at $x = 1$, thus invalidating the assumption leading to Eq. (19). For $\omega_0 = 1$, $x = \exp(-\omega_0/2) = 0.606530660$. This point is shown in Fig. 2 as N. This endpoint is the end of a line of fixed points. Because the equations of motion are linear in this example, the tangent map, or monodromy matrix, is just $M(1^+ \leftarrow 0^+)$. These fixed points are of parabolic type since $\text{Tr}\, M(1^+ \leftarrow 0^+) = 2$.

Another simple example is when the particle starts at $x_0 = 0$ moving toward the wall at $x = 1$ with an appropriate positive momentum p_0, so that it bounces between the two walls several times and, at exactly half a period, the particle comes back to its initial position at $x = 0$. This case is shown in Fig. 3. Because $x = 0$, the particle does not feel the δ-kicks, and the motion is periodic. Note that the particle has to travel from $x = 0$ to $x = 1$ in a time $t = 1/4n$, with $n = 1, 2, \ldots$. The cases $n = 1$ and $n = 2$ are shown in Fig. 3. To calculate the corresponding initial momenta p_0, we use Eq. (14) with $x(t_0) = 0$, $x(t) = 1$, $p(t_0) = p_0$, $t' = 1/4n$, and $E = p_0^2/2$, getting

$$p_0 = \frac{\omega_0}{\sinh(\omega_0/4n)}, \qquad n = 1, 2, \ldots \tag{20}$$

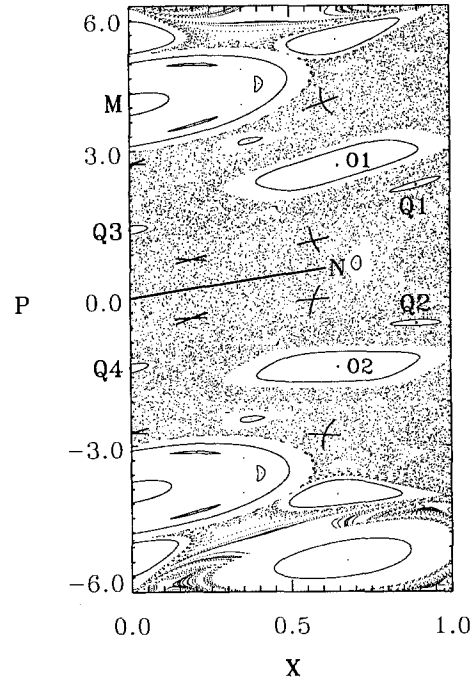

Fig. 2. Classical stroboscopic phase space plot for $\omega_0 = 1$. The chaotic background is obtained from a single initial condition. On the empty islands there are KAM curves around the elliptic periodic orbits. The straight line, starting at (0, 0) and ending at N, denotes parabolic fixed points. A hyperbolic period-7 periodic orbit embedded in the chaotic background is marked by crosses at the intercept of the stable and unstable manifolds. The remaining points indicated by letters are explained in the text.

For $\omega_0 = 1$, and $n = 1$, $p_0 = 3.958635163$. This point is shown in Fig. 2 and is denoted as M. Since the monodromy matrix in the present case is hard to obtain analytically, we studied the problem numerically for $\omega_0 = 1$. We find KAM curves around these periodic orbits, which leads us to conclude that, for $\omega_0 = 1$, this is a family of elliptic periodic orbits.

We proceed to calculate a nontrivial period-2 orbit, shown in Fig. 4. Suppose that the particle starts from the initial position x_0 and momentum p_0 (>0) (denoted as point a in Fig. 4), with energy $E_0 = (p_0^2 - \omega_0^2 x_0^2)/2$. The values of (x_0, p_0) are such that, in the first half period of free propagation, the particle bounces off the wall at $x = 1$ (denoted as point b in Fig. 4), reverses direction, and hits the wall at $x = 0$ exactly at half a period (shown as point c in Fig. 4). At $x = 0$ the kick is absent. In the second half period of free propagation, the particle bounces off the wall at $x = 1$ and comes back to $x = x_0$ with negative momentum $p = -p_0$. This second half

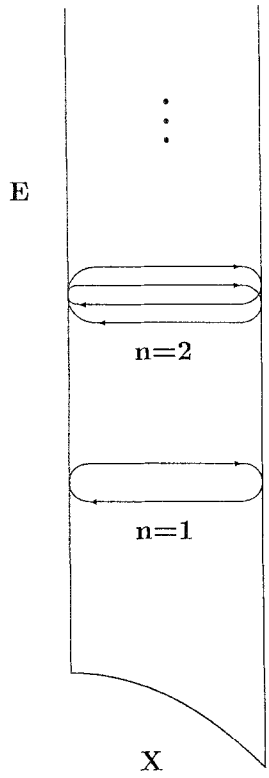

Fig. 3. A family of periodic orbits shown schematically in energy–position space. Arrows refer to the directions of momentum. See text for more explanation of this figure.

period of free propagation is simply the time-reversed motion of the first half period of free propagation. The kick at full period leaves the particle with a smaller negative momentum equal to $-p_0+2\omega_0 x_0$, and thus a lower energy $E=[(-p_0+2\omega_0 x_0)^2-\omega_0^2 x_0^2]/2$ (shown as point d in Fig. 4). The third half period of free propagation results in the particle hitting the wall at $x=0$ (denoted as point e in Fig. 4). The fourth half period of free propagation brings the particle back to $x=x_0$ with a positive momentum $p=p_0-2\omega_0 x_0$. This is just the time-reversed motion of the third half period of free propagation. Finally, the last kick sends the particle back to its initial position and momentum (x_0, p_0), and thus completes its full periodic motion. We now derive the constraint equations for the initial conditions (x_0, p_0) so as to generate this type of period-2 orbit. The time needed to travel from one wall to the other is $t'=\sinh^{-1}[\omega_0/(2E_0)^{1/2}]/\omega_0$, for a particle with energy E_0. This result is obtained from Eq. (14) by setting $x(t_0)=0$, $p(x_0)=(2E_0)^{1/2}$, and $x(t)=1$. To hit the wall at $x=1$,

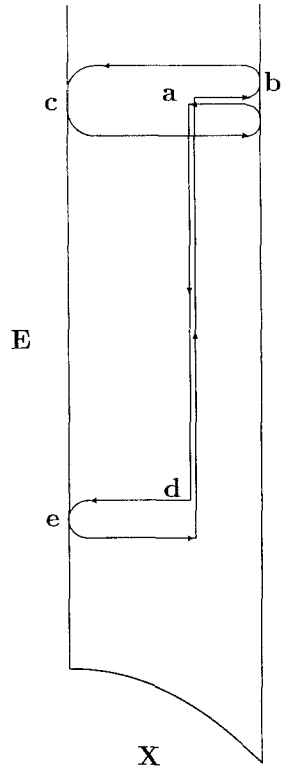

Fig. 4. Nontrivial period-2 orbit shown schematically in energy–position space as in Fig. 3. See text for the definition of points *a*, *b*, *c*, *d*, *e*.

the time needed by the particle to follow the periodic motion described above will be $1/2-\sinh^{-1}[\omega_0/(2E_0)^{1/2}]/\omega_0]$ (from point a to point b in Fig. 4). The momentum at $x=1$ is $(2E_0+\omega_0^2)^{1/2}$ from conservation of energy. Substituting these values into Eq. (14), one gets

$$p_0-x_0(2E_0+\omega_0^2)^{1/2}=\frac{2E_0}{\omega_0}\sinh\left[\frac{\omega_0}{2}-\sinh^{-1}\left(\frac{\omega_0}{(2E_0)^{1/2}}\right)\right] \tag{21}$$

In the third half period of free propagation, in order to have the particle go from point d to point e in Fig. 4, x_0 must be given by

$$x_0=\frac{(2E)^{1/2}}{\omega_0}\sinh\left(\frac{\omega_0}{2}\right) \tag{22}$$

This result is derived from Eq. (14) after setting $x(t_0)=x_0$, $x(t)=0$, $p(t)=(2E)^{1/2}$, and $t'=1/2$ with E_0 and E as defined before. This set of

coupled equations (21) and (22) might not yield physical solutions (i.e., with $0 \leqslant x_0 \leqslant 1$) for general values of ω_0. There is a physical solution with $x_0 = 0.649092519$, and $p_0 = 2.702791010$, for $\omega_0 = 1$, though. This is point a in Fig. 4. The position and momentum at full period are x_0 and $-p_0 + 2\omega_0 x_0$, with the value of the latter being equal to -1.404605972. This is point d in Fig. 4. Points a and d are shown in Fig. 2 as O_1 and O_2, respectively. Note that these two points are symmetric with respect to the line of fixed points terminating at the endpoint N in Fig. 2. We shall come back to this point in Section 5. We find, again numerically, that these points also represent elliptic periodic orbits. Equations (21) and (22) can be generalized to describe a family of periodic orbits, at exactly half period, where the particle bounces back and forth several times before it hits the wall at points c and e in Fig. 4. Taking this into consideration, Eqs. (21) and (22) are generalized to

$$\begin{aligned} p_0 - x_0(2E_0 + \omega_0^2)^{1/2} &= \frac{2E_0}{\omega_0} \sinh\left[\frac{\omega_0}{2} - (2n+1)\sinh^{-1}\left(\frac{\omega_0}{(2E_0)^{1/2}}\right)\right] \\ x_0 &= \frac{(2E)^{1/2}}{\omega_0} \sinh\left[\frac{\omega_0}{2} - (2m+1)\sinh^{-1}\left(\frac{\omega_0}{(2E)^{1/2}}\right)\right] \end{aligned} \tag{23}$$

with $m, n = 0, 1, 2, \ldots$, and the only physical solutions are those for which $0 \leqslant x_0 \leqslant 1$.

The calculations of these period-2 orbits and their generalizations are just examples of how one can study a class of periodic orbits analytically. For arbitrary periodic orbits, this procedure may involve a larger set of coupled nonlinear equations than those in Eqs. (21) and (22) or (23). In principle, however, most periodic orbits could be calculated this way. In practice this is not possible except in simple cases like the ones discussed above. We note that this type of analytic analysis is useful in checking the results obtained numerically. For example, we checked the numerical algorithm used in obtaining the results discussed in Section 5 against these analytical calculations. We found that our numerical calculations matched the analytical results discussed above up to eight significant digits, which is sufficient for our purposes in this paper.

4. QUANTUM STUDY

The spectrum of the Hamiltonian operator plays the central role in studies of time-independent problems. Similarly, when the Hamiltonian is periodic in time, the central issue is calculating the spectral properties of the one-period Floquet operator. The Floquet operator is the quantum counterpart of the classical one-period map given in Eq. (18). One can

simply carry out the canonical quantization of Eq. (12) as usual, and the quantum version of Eq. (18) gives the Floquet operator

$$\hat{U}(1^+ \leftarrow 0^+) = \exp\left(i\frac{\omega_0}{\hbar}\hat{x}^2\right)\cdot\exp\left(-i\frac{\hat{H}_0}{2\hbar}\right)$$
$$\cdot\exp\left(-i\frac{\omega_0}{\hbar}\hat{x}^2\right)\cdot\exp\left(-i\frac{\hat{H}_0}{2\hbar}\right) \tag{24}$$

with $\hat{H}_0 = \hat{p}^2/2 - \omega_0^2\hat{x}^2/2$, and $0 \leqslant x \leqslant 1$. The Floquet operator $\hat{U}(1^+ \leftarrow 0^+)$ contains four parts as in the classical map of Eq. (18), i.e., two half-period free propagation and two Dirac-δ kicks, one at half and the other at full period. In the classical case, in order to take care of the boundary conditions at $x=0$ and $x=1$, the matrix for free propagation M_{f}, may contain a product of many M_0 and M_{wall} matrices. In contrast, in the quantum operator case the free propagation at half period entails just one matrix, $\exp(-i\hat{H}_0/2\hbar)$. This is characteristic of a quantum problem where the particle, although free, still "feels" the boundary conditions at all times. When the particle propagates freely, the basis spanning the Hilbert space is formed by the eigenfunctions of the inverted harmonic oscillator confined to a box. In this limit the Schrödinger equation for $\hat{H}_0$, in dimensionless units, reads

$$\frac{d^2}{dz^2}\Psi(z) + \left(\frac{z^2}{4} - a\right)\Psi(z) = 0 \tag{25}$$

where $z = x(2\omega_0/\hbar)^{1/2}$, $a = -E/\hbar\omega_0$, and E is the eigenenergy of $\hat{H}_0$. This is Weber's equation with $\Psi(z)$ the parabolic cylinder functions.[18] The eigenenergies and eigenfunctions are obtained by imposing the boundary conditions

$$\Psi_a(z=0) = \Psi_a(z=(2\omega_0/\hbar)^{1/2}) = 0 \tag{26}$$

Note that the ith eigenfunction $\Psi_{a_i}(x)$ depends only on the parameter $\omega_0/\hbar$, and the corresponding eigenenergy $E_i = -\hbar\omega_0 a_i(\omega_0/\hbar)$ depends on both $\hbar\omega_0$ and $\omega_0/\hbar$. Notice that the second boundary condition in Eq. (26) is such that in the large-$\hbar$ limit the box can be well approximated by a flat box with standard sinusoidal solutions, while in the small-$\hbar$ regime, of interest here, the inverted oscillator potential becomes dominant, mostly close to $z = (2\omega_0/\hbar)^{1/2}$.

The explicit calculations of the parabolic cylinder functions $\Psi_{a_i}(x)$ in the semiclassical regime cannot be done efficiently using their standard power series expansions in z. Instead, we find it convenient to diagonalize $\hat{H}_0$ on the complete set of the Fourier sinusoidal basis. One then expands

$\Psi_{a_i}(x)$ in the sine basis. The number of terms needed in the expansion to get a good approximation to $\Psi_{a_i}(x)$ is a function of $\hbar$. The smaller the $\hbar$, the larger the number of terms needed in the expansion.

The solution to the time-dependent problem is obtained from solving the eigenvalue equation for the Floquet operator

$$\hat{U}\,|\psi\rangle = e^{i\varphi}\,|\psi\rangle \tag{27}$$

where $|\psi\rangle$ is the quasienergy eigenstate, and φ its quasienergy eigenvalue.[19] To obtain the spectral properties of the Floquet operator, we diagonalized $\hat{U}$ using as a basis the parabolic cylinder functions $\Psi_{a_i}(x)$ obtained from the diagonalization of $\hat{H}_0$.

To compare the quantum map results to the classical ones, we need to have a phase-space representation of the quasienergy eigenfunctions. A convenient way to do this is to use the Husimi representation of the quasienergy eigenfunctions with the minimum-uncertainty Gaussian wave packet

$$\langle x|\,\alpha(x_0, p_0)\rangle = \left(\frac{\sigma}{\pi\hbar}\right)^{1/4} \exp\left[-\frac{\sigma}{2\hbar}(x-x_0)^2 + i\frac{p_0}{\hbar}\left(x-\frac{x_0}{2}\right)\right] \tag{28}$$

centered at (x_0, p_0) in phase space. Here the root mean square deviations $\Delta x = (\hbar/2\sigma)^{1/2}$ and $\Delta p = (\hbar\sigma/2)^{1/2}$ are such that $\Delta x\,\Delta p = \hbar/2$, with σ the squeezing parameter used when adjusting Δx and Δp to make comparisons to classical phase-space plots. The Husimi distribution of a quasienergy eigenfunction $|\psi\rangle$ is given by the absolute value square of the inner product of the minimum-uncertainty Gaussian wave packet with $|\psi\rangle$,[6] i.e.,

$$\mathscr{F}_\psi(x_0, p_0) = |\langle\psi\,|\,\alpha(x_0, p_0)\rangle|^2 = \left|\int_0^1 \langle\psi\,|\,x\rangle\langle x\,|\,\alpha(x_0, p_0)\rangle\,dx\right|^2 \tag{29}$$

The Husimi distribution function $\mathscr{F}_\psi$ is obtained by scanning the values of (x_0, p_0) through a region of interest in phase space. The resulting distribution is then used to compare to the stroboscopic trajectories in phase space obtained from the classical analysis.

As mentioned in Section 3, the only free parameter in the classical analysis is ω_0. In contrast, the quantum Floquet operator (24) depends on $\hbar$ and ω_0 explicitly as $\omega_0/\hbar$ and $\hat{H}_0/\hbar$. Since the basis functions Ψ_{a_i} depend on $\omega_0/\hbar$ only, and the eigenenergies $E_i = -\hbar\omega_0 a_i(\omega_0/\hbar)$, the Floquet operator (24) depends on the parameters $\hbar$ and ω_0 only through $\omega_0/\hbar$ and ω_0. This parameter dependence gives a crucial difference between the Fermi and FIPO representations. In the Fermi case the Floquet operator

depends only on $\omega_0/\hbar$.[4,9] This makes the connection to the classical limit difficult.[9] The reason for this difference in the parameter dependences is because the time-dependent transformation given in Eq. (7) changes the dynamics in an essential way. This transformation is analogous to changing from a fixed to a rotating frame in the problem of a charge in a constant magnetic field.

5. NUMERICAL RESULTS

To discuss our classical and quantum results, we start by identifying the special symmetry that was briefly mentioned after Eq. (22). The classical dynamics described by Eq. (12) consists of free-particle propagation between δ-kicks or collisions with the walls. The δ-kick potentials act every half period and are of opposite signs. At kick time, say at $t=0$, the continuity conditions yield $x(0^+)=x(0^-)$ and $p(0^+)=p(0^-)+2\omega_0 x(0)$. If we define $x(t=0^+)=x_0$and $p(t=0^+)=p_0$, then at time $t=0^-$ the particle, although located at the same point in space, had momentum $-p(t=0^-)=2\omega_0 x_0-p_0$. Since the Hamiltonian given in Eq. (12) is even in time, propagating the point (x_0, p_0) into the future would be the same as propagating it from the past to the point $(x_0, 2\omega_0 x_0-p_0)$. Because t and $-t$ should lead to the same answer, we should have a symmetry about the line $p=\omega_0 x$. This symmetry line coincides with the line of parabolic fixed points shown in Fig. 2 and extends to $x=1$. This symmetry line is preserved in the quantum problem. It is shown in the quantum phase-space examples of Husimi plots in Figs. 5–8.

The numerical calculations were done for the most with the parameter $\omega_0=1$. In this case the two potential terms in the Hamiltonian (12) are comparable in magnitude. We also did calculations for values of $\omega_0=1.2, 0.8,$ and 0.5, and both classical and quantum results are qualitatively the same as those obtained from the calculations with $\omega_0=1$.

In the classical analysis we used the map (18) to produce the stroboscopic phase space plots shown in Fig. 2. First we calculated 40,000 iterations from a single initial condition, say $x=0.2$, $p=-2.0$. This initial condition leads to a chaotic trajectory shown as a background in Fig. 2 and plotted in the range $p\in[-6, 6]$. The islands in the middle of the chaotic orbit are Kolmogorov–Arnold–Moser (KAM) curves surrounding elliptic periodic orbits. The KAM curves are calculated after choosing appropriate initial conditions. The points in the middle of the KAM curves correspond to elliptic periodic orbits. The analytic calculation of the points M, O_1, and O_2 shown in Fig. 2 was discussed in Section 3. The other elliptic points denoted by Q_1, Q_2, Q_3, and Q_4 in Fig. 2 were found numerically. The straight line that starts from (0, 0) and ends at N in Fig. 2 is the line

of parabolic fixed points discussed in Section 3. This line also coincides with the symmetry line $p = \omega_0 x$ for $x < 0.606530660$. The hyperbolic periodic orbits marked as crossed lines in Fig. 2 denote stable and unstable manifolds embedded in the chaotic sea and were also determined numerically. These orbits were found as follows. We took thousands of initial conditions along a line, either the symmetry line $p = \omega_0 x$ or the boundary line $x = 0$. Next we iterated these initial conditions for a few periods to see if these lines came back and crossed the initial line. If they did not, there may not be periodic orbits along the initial line for these time periods. If they did cross the initial line, we reduced the range of initial conditions further and further to pin down the periodic orbits up to eight significant digits. If these periodic orbits were unstable for thousands of iterations, we call them hyperbolic. The monodromy matrix is then calculated about a small neighborhood of these hyperbolic periodic orbits. Stable and unstable manifolds are then obtained through the iterations of the initial conditions along the eigenvectors of the monodromy matrix. In Fig. 2, we show a hyperbolic period-7 orbit, denoted by intersections of stable and unstable manifolds.

In the quantum study we fixed $\omega_0 = 1$ as in the classical case and chose values of $\hbar$ and n (the dimension of the truncated U matrix). Next we diagonalized the U matrix to obtain its quasienergy spectra. In choosing the values of $\hbar$ and n, we observe that n has to be such that the maximum value of the eigenenergy of $\hat{H}_0$ has to be larger than the maximum energy of the classical trajectory in the region $p_{\max}^2/2$. Here $p_{\max}$ is the maximum phase-space momentum of interest. In the plots shown in Fig. 2, $p_{\max} = 6$. Otherwise the portion of the phase space of interest is not fully covered by the quantum mechanical calculation. From the numerical analysis point of view, the smaller the $\hbar$, the bigger the off-diagonal matrix elements in $\hat{H}_0$, in the sinusoidal basis, and the larger the n value should be to achieve accuracy in the calculations of the parabolic functions. After several tries we chose $\hbar = 0.012$ and $n = 150$ as optimal parameter values. For $\hbar$ smaller than this value a larger n has to be used. Furthermore, we found that for these parameter values a clear connection between the classical and quantum solutions is achieved. Thus we do not expect qualitative changes in our results from considering matrices one order of magnitude larger than the ones considered here.

In calculating the Husimi distributions of the quasienergy eigenfunctions [see Eq. (29)], we scanned the (x_0, p_0) values through the region of phase space of interest using a grid of 60×80 points. The resulting Husimi distributions $\mathcal{F}_\psi(x_0, p_0)$ are shown as contour plots in Figs. 5–8, with the value of Planck's constant h annotated at the upper right-hand corner in the figures.

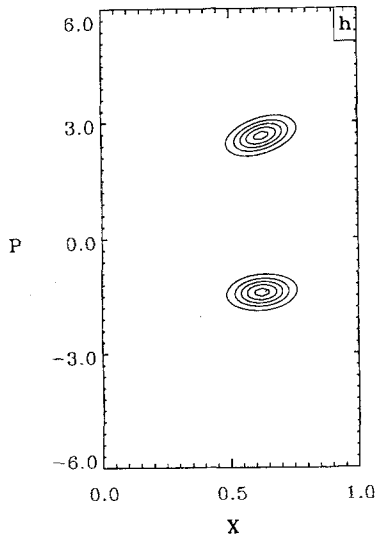

Fig. 5. Contour plot of a Husimi distribution of a quasienergy eigenfunction corresponding to the elliptic periodic orbits O_1 and O_2 shown in Fig. 2.

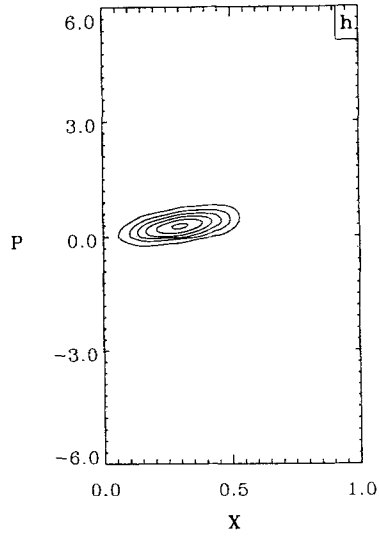

Fig. 6. The same as in Fig. 5 corresponding to the parabolic fixed points shown in Fig. 2.

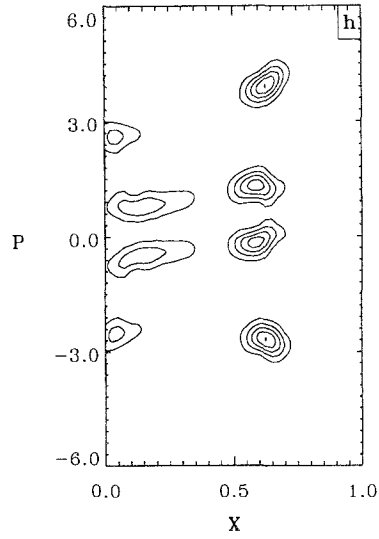

Fig. 7. Same as in Fig. 5 for the hyperbolic periodic orbit marked by its stable and unstable manifolds in Fig. 2. These structures are referred to as "scars" in the literature.

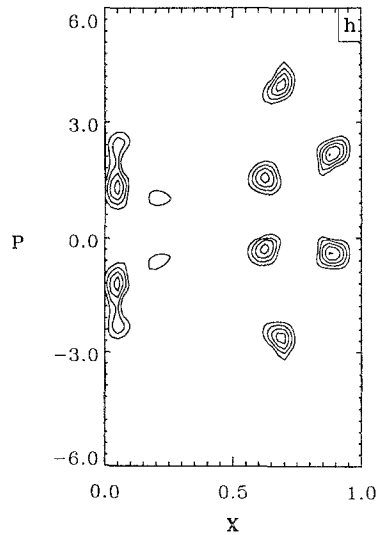

Fig. 8. Same as in Fig. 5 corresponding to the two periodic orbits, one elliptic, denoted by Q_1, Q_2, Q_3, and Q_4 in Fig. 2, the other a hyperbolic orbit marked by its stable and unstable manifolds in the same figure.

Next we compare examples of Husimi distributions to the classical solutions shown in Fig. 2. We note first that there are clear structures in $\mathcal{F}_\psi(x_0, p_0)$ that correspond to the classical elliptic, parabolic, and hyperbolic periodic orbits shown in Fig. 2. Specifically, Fig. 5 shows the Husimi distribution of a quasienergy eigenfunction whose classical counterpart is the elliptic periodic orbits O_1 and O_2 shown in Fig. 2. Figure 6 shows $\mathcal{F}_\psi(x_0, p_0)$ for a quasienergy eigenfunction which corresponds to parabolic fixed points. Figure 7 shows the Husimi distribution for a quasienergy eigenfunction corresponding to the period-7 hyperbolic periodic orbit marked by its stable and unstable manifolds in Fig. 2. The structures in the Husimi distributions shown in Fig. 7 are referred to as "scars" in the literature.[6,7,20,21] These are defined as enhanced wavefunction probability densities in the Husimi distributions about hyperbolic classical periodic orbits. Since hyperbolic periodic orbits play an important role in classical chaos, one expects that the "scars" may also play an important role in sorting out the QMCC. Thus understanding of the meaning of "scars" may be important in understanding the QMCC. Finally, in Fig. 8 we show the Husimi distribution of a single quasienergy eigenfunction having a clear structure around two periodic orbits. One is a period-4 elliptic orbit shown in Fig. 2 as Q_1, Q_2, Q_3, and Q_4, and the other is the period-7 hyperbolic orbit marked by its stable and unstable manifolds. This type of solution is a purely quantum mechanical result and relates the quantum tunneling between elliptic regions in phase space. This tunneling effect between the classical elliptic and hyperbolic orbits through KAM curves has been observed in other classically chaotic system.[7,22] This feature implies that the correspondence between the classical orbits and the Husimi distributions of the eigenfunctions is not one to one, and the mixing of the elliptic and hyperbolic types in quantum mechanics is a major difference with respect to classical mechanics. Out of the 150 Husimi distributions we calculated, about 40% clearly correspond to elliptic classical periodic orbits, about 20% to hyperbolic orbits, and 2 or 3 are parabolic and 3 or 4 correspond to tunneling events between elliptic and hyperbolic orbits. There are Husimi distributions that cannot be identified to any of the above types, although they are rather well defined in phase space. When the period is less than 10, the Husimi distributions can be clearly identified. One difficulty in connecting all the quantum Husimi distributions to specific classical periodic orbits is that we do not have the full classification of all the classical orbits, including the ones that are not periodic. A full classical analysis of all possible solutions would be a very difficult task to carry out though.

6. CONCLUSIONS

This paper has presented a direct connection between the classical and quantum solutions of the Fermi acceleration model in its finite inverted parametric oscillator (FIPO) representation. The connection was exhibited for generic special solutions identified both in the classical and quantum mechanical limits. The quantum quasienergy solutions were analyzed in their Husimi phase-space representation. Examples of elliptic, parabolic, and hyperbolic orbits were connected directly to their quantum counterparts. Of particular note are the Husimi distributions shown in Figs. 7 and 8, where "scars" and coexisting hyperbolic and elliptic regions are shown. The former represents an increased probability density, or phase space localization, about the isolated hyperbolic periodic orbits in the sea of chaos. The latter is due to tunneling events, forbidden classically, through the dynamical barriers produced by the KAM surfaces.

ACKNOWLEDGMENTS

We thank the Donors of the Petroleum Research Fund, administered by the American Chemical Society, under grant ACS-PRF#22036-AC6, and the Office of Naval Research for the partial support of this research.

REFERENCES

1. T. H. Seligman and H. Nishioka, eds., *II International Conference on Quantum Chaos* (Springer-Verlag, 1986).
2. O. Bohigas, M. J. Giannoni, and C. Schmit, *Phys. Rev. Lett.* **52**:1 (1984).
3. M. Mehta, ed., *Random Matrices: An Enlarged and Revised Second Edition* (Academic Press, 1991).
4. J. V. José and R. Cordery, *Phys. Rev. Lett.* **56**:290 (1986).
5. F. M. Izrailev, *Phys. Rev. Lett.* **56**:541 (1986).
6. S. J. Chang and K. J. Shi, *Phys. Rev. A* **34**:7 (1986); G. Radons and R. E. Prange, *Phys. Rev. Lett.* **61**:1691 (1988).
7. R. V. Jensen, M. M. Sanders, M. Saraceno, and B. Sundaram, *Phys. Rev. Lett.* **63**:2771 (1989); W. A. Lin and L. E. Ballentine, *Phys. Rev. Lett.* **65**:2927 (1990).
8. M. A. Lieberman and A. J. Lichtenberg, *Phys. Rev. A* **5**:1852 (1971).
9. W. M. Visscher, *Phys. Rev. A* **36**:5031 (1987).
10. E. Fermi, *Phys. Rev.* **75**:1169 (1949).
11. R. Bellman, *Perturbation Techniques in Mathematics Engineering & Physics* (Dover, New York).
12. L. S. Schulman, *Techniques and Applications of Path Integration* (Wiley, 1981).
13. A. Munier, J. R. Burgan, M. Feix, and E. Fijalkow, *J. Math. Phys.* **22**:1219 (1981).
14. M. V. Berry and G. Klein, *J. Phys. A: Math. Gen.* **17**:1805 (1984).
15. L. Chetouani, L. Guechi, and T. F. Hammann, *Phys. Rev. A* **40**:1157 (1989).
16. S. Takagi, *Prog. Theor. Phys.* **84**:1019 (1990).

17. P. Seba, *Phys. Rev. A* **41**:2306 (1990).
18. M. Abramowitz and I. A. Stegun, *Handbook of Mathematical Functions* (Dover, 1972).
19. Ya. B. Zel'dovich, *Sov. Phys.-JETP* **24**:1006 (1967).
20. E. J. Heller, *Phys. Rev. Lett.* **53**:1515 (1984).
21. R. L. Waterland, J. M. Yuan, C. C. Martens, R. E. Grillian, and W. P. Reinhardt, *Phys. Rev. Lett.* **61**:2733 (1988).
22. R. Geisel, G. Radons, and J. Rubner, *Phys. Rev. Lett.* **57**:2883 (1986).